

# Aeroacoustic Testing of Open Rotors at Very Small Scale

Alexander Truong<sup>1</sup> and Dimitri Papamoschou<sup>2</sup>  
*University of California, Irvine, Irvine, CA 92697*

**This study examines the potential of very-small-scale experiments to simulate the acoustics of large scale counter-rotating open rotors in isolation and with a rectangular-plate shield. The experimental rotor model was based on the historical F7/A7 design developed by General Electric. The 80-mm diameter rotors were fabricated using advanced stereolithography and were powered by two high-performance DC brushless motors. Realistic tip Mach numbers were achieved with the rotors spinning near 50000 rpm. Far-field acoustic surveys were conducted inside an anechoic chamber using a 12-microphone array. The isolated tests captured the tonal and broadband contents of open rotor noise. Rotor-alone tones dominated the sound emission in the vicinity of the rotor plane. In the aft direction, interaction tones were very strong. Addition of the rectangular plate shield created complex trends in the tonal content. Tones radiating in the direction of the rotor plane were well attenuated, while tones emitted in the aft direction were poorly shielded. Some tones were amplified with insertion of the shield. Even though the shield reduced the noise level in an overall sense, the complicated tonal pattern presents challenges for the effective reduction of aircraft noise.**

## I. Introduction

Rising fuel costs and environmental concerns have reinvigorated the open rotor concept for aircraft propulsion. The concept was investigated extensively in the 1970s and 1980s, culminating with the flight testing of the GE36 unducted fan engine on Boeing 727 and McDonnell Douglas MD80 aircraft<sup>1</sup>. Research programs at NASA and industry resulted in a large number of reports on the aerodynamic performance and noise emission of open rotors, with emphasis on counter-rotating concepts<sup>2-6</sup>. While the propulsive-efficiency advantage of the counter-rotating open rotor, over a conventional turbofan engine, is unquestionable, installation, noise, and image problems beset the concept and it did not find commercial application. Perhaps the most vexing problem is the community noise caused by the rich tonal content of the counter-rotating open rotor. Present efforts include modeling and reducing the noise of the isolated rotor<sup>7-9</sup>, as well as exploring airframe-propulsion integration concepts that may result in a quieter system<sup>10,11</sup>. The latter includes an open-rotor version of the hybrid-wing-body (HWB) airplane where the placement of the engine over the wing is exploited to shield downward-emitted noise<sup>12,13</sup>.

Subscale experimental tests of open rotors have occurred primarily at NASA wind tunnels (e.g., Refs. 5,6). These are state-of-the art facilities featuring pneumatic motors for powering the rotors and acoustic instrumentation that permits noise surveys as well as noise source location. The typical rotor diameter investigated is ~0.6 m, which about 1/5-1/7 of the scale of a rotor on a large commercial airliner. These experiments are obviously very expensive. Due to the complexity and cost of the rotor hardware, only a small number of parameters can be varied within a reasonable budget. This limits the parameter space and the number of innovative ideas that can be tested.

The advent of stereolithographic fabrication methods enables the three-dimensional “printing” of complex, small-scale objects with high resolution. For an intricate design like a propeller, the manufacturing costs are orders of magnitude lower than fabricating the same article using conventional machining. This would permit the investigation of a large number of concepts at small cost, identifying promising configurations that may merit testing at larger scale and filtering out ideas that do not show promise. The rapid-prototyping approach has been used successfully with jet noise testing of complex nozzle configurations<sup>14</sup>. The propeller presents the challenges of very fine trailing edge thickness, severe stress environment due to the very large rotational speeds required of a small-scale apparatus, and powerplant selection. Even though the scale is very small (in this study it is about 1/50th of full scale), the power requirements for realistic conditions are on the order of a few horsepower and are thus non-trivial. Selection of the power plant type should be compatible with the scope of this effort, i.e., not overly complex or expensive. The optimal solution appears to be the use of motors and power sources used in electric radio-

<sup>1</sup> Junior Specialist, Department of Mechanical and Aerospace Engineering, adtruong@uci.edu, Member AIAA.

<sup>2</sup> Professor, Department of Mechanical and Aerospace Engineering, dpapamos@uci.edu, Fellow AIAA.

controlled airplanes. The power plants are characterized by very high power densities delivered over a short time. Acoustic testing only requires short test times, therefore the RC motors are well suited for this purpose.

This paper describes an initial, internally-funded effort at addressing the above questions, i.e., whether the fabrication and testing of rotors at very small scale is technically feasible and produces realistic acoustics data. In addition, a small parametric study of rotor noise shielding was undertaken.

## II. Rotor Design

### A. Rotor Specifications and Geometry

The counter-rotating propeller configuration of this study was patterned after the General Electric F7/A7 rotor studied extensively in experiments at NASA facilities<sup>5,6</sup>. The basic F7/A7 had eight blades for the front and aft rotors (8+8 configuration). Information in the open literature provides details on the distribution of stagger angle, camber angle, thickness ratio, chord, and axial and tangential distances from the pitch change axis<sup>2</sup>. However, the specifics of the airfoil profile were not included. Several studies emphasized a generic selection of the blade airfoil<sup>4,9</sup>, using NACA 65-series from the root to 40% percent of the blade that then transitioning to NACA 16-series airfoil. With this information regarding the aerodynamic profile, stacking characteristic, and airfoil geometry data, a realistic rotor can be synthesized.

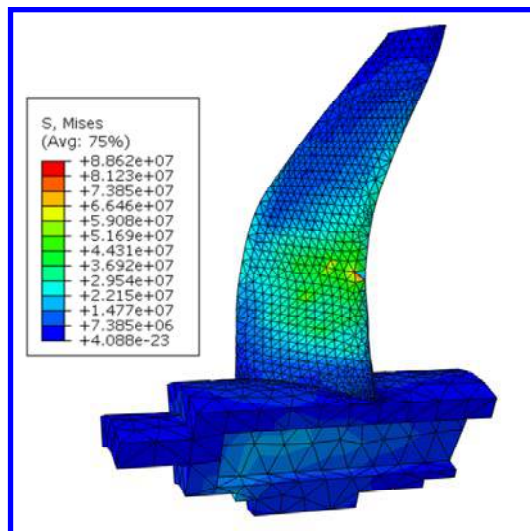
In scaling down the rotor, the primary criterion was maintaining a tip speed similar to that of the full-scale rotor. This determines a relation between rotor diameter and rotational velocity. The sizing of the rotor is dictated by the availability of motors compatible with the scale of this effort. Some of the most powerful brushless DC motors used in radio-controlled aircraft achieve powers on the order of 2 kW and have an RPM/Volt rating on the order of 5000. The power limit, combined with the typical open-rotor pressure ratio of 1.05, leads to a rotor diameter of around 50-100 mm. The tip speed and RPM/Volt rating narrows this further to around 70-90 mm. Using this process, the rotor diameter chosen was  $D=80$  mm. The required RPM for tip Mach number of 0.65 was 53,000.

The F7/A7 geometry given in the aforementioned reports is based on forward flight, typically at cruise Mach number. The present experiment, which was static, required a reduction in blade pitch angle to prevent blade stall. This was achieved by using blade element theory (BET) with an angle of attack criterion of  $4^\circ$ . Accordingly, the tip pitch angles were  $12.8^\circ$  and  $10.4^\circ$  for the forward and aft rotors, respectively. These values are about  $25^\circ$  smaller than for the large-scale rotors tested at Mach 0.2. Thrust measured using a small test stand with a force transducer was in agreement with the prediction of the BET.

Manufacturing and structural concerns arose due to the thin nature of the blades. Thicknesses below 0.4 millimeters (0.016 inches) strained the capability of rapid prototyping machines and the articles would not form properly. Also, the rapid-prototyping material becomes fragile for very small thickness. Structural concerns were that the blades would fail due to the centrifugal force of operating at up to 60000 rpm. In response, the blade profiles were structurally modified. Figure 1 illustrates the alterations made to the airfoil profile, notably the increased thickness at the leading and trailing edges. The trailing edge thickness depends on the radial position of the section. Various trailing edge thickness profiles were designed and stress tested using Abaqus finite element analysis software (Dassault Systemes). Von Misses stress distributions of the final design operating at 60000 RPM are shown in Fig. 2. The final design utilized a trailing edge thickness of 0.7 mm at the root gradually reducing to 0.4 mm at the tip. The safety factor was approximately 1.2.

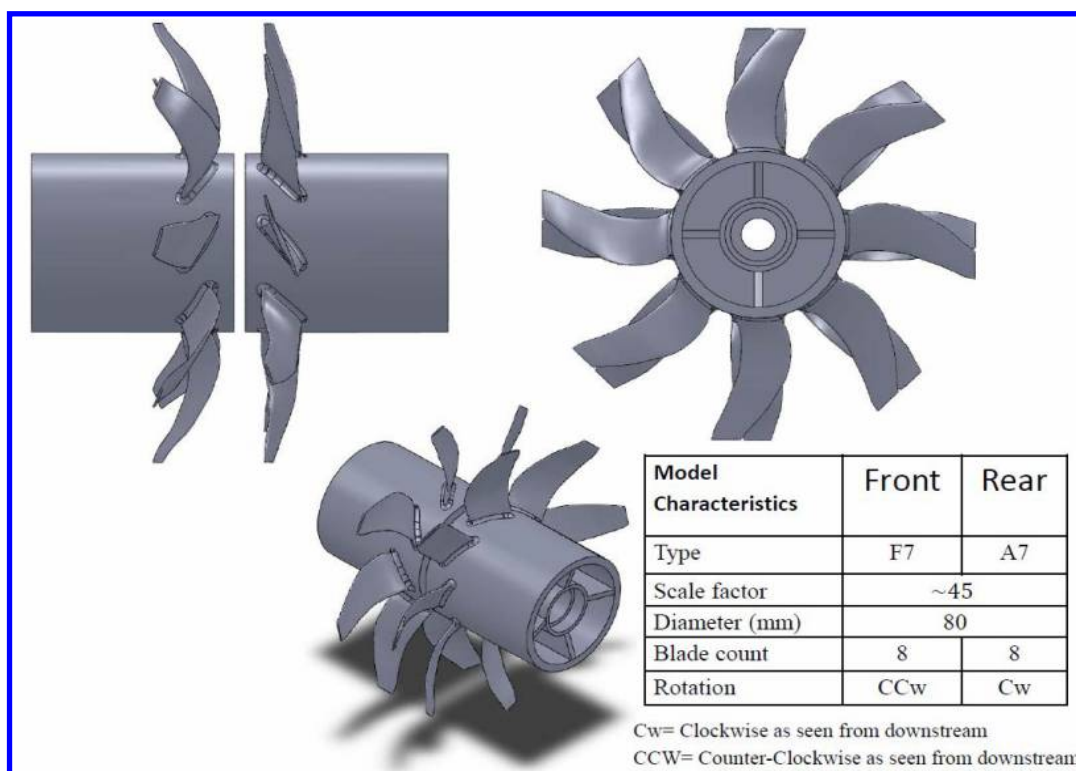


Fig.1 Changes in the thickness profile. The red line represents the original configuration, while the blue line represents the modified airfoil.



**Fig.2 Von Mises stress distribution (MPa) in the final rotor design.**

The final rotor design is depicted in Fig. 3. The rotor diameter was  $D=80$  mm and the hub-to-tip radius was  $d/D=0.398$ . The rotor spacing between pitch change axes was  $\Delta x/D=0.2$ , or  $\Delta x=16$  mm. The blade geometry was imported into SolidWorks CAD software (Dassault Systemes), as shown in Fig. 3. Stereolithography files were generated, and fabrication was done by Fineline Corporation using 3D Systems’ Viper High Resolution SLA machine. The material was Accura 60 resin by 3D Systems with tensile modulus of  $\sim 3000$  MPa. The rotor blades were hand-finished to a highly smooth and polished surface using 12000-grit sandpaper. Figure 4 shows a photograph of the rotors tested.



**Fig. 3 CAD model of the open rotor pairs.**



**Fig. 4 Rapid-prototyped rotors.**

### **III. Experimental Setup**

#### **A. Counter-Rotating Rotor Apparatus**

Small-scale acoustic simulation of the open rotor used a counter-rotating rig shown in Fig. 5. The rig consisted of two rotors spinning in opposite directions. Each rotor was powered separately by a brushless DC motor. Each motor was enclosed in an aluminum hubs supported by stainless steel struts. The struts were mounted on two steel rods which enabled control of the spacing between the two rotors.

The two brushless DC motors were Hoffman Magnetics EDF 70 HW “Wild Beast” with maximum power output each of 1700 W and RPM/Volt rating of 5000. They were independently controlled using Castle Creations Phoenix 125-Amp electronic speed controller (ESC). The ESC can function on a continuous current of 125 amps and a surge current of 160 amps at 14.8 Volts. Power to the speed controller was supplied by a 4S (14.8-Volt) lithium-ion polymer (Lipo) battery with discharge rate of 30 C and capacity of 5000 mAh. The speed controller was controlled by a Spektrum AR6200 DSM2 6 channel receiver connected wirelessly to a Spektrum DX7 2.4 GHz seven-channel radio. The receiver was powered by a Castle Creations battery eliminator circuit (BEC). Figure 6 outlines the electronic circuitry.

Rotor speed was obtained through electronic means, using the process of Fig.7. Inputs to the RPM sensor required a voltage signal from any two wires leading from the ESC to the motor. The raw signal voltage was reduced to levels tolerated by the data acquisition systems. A buffer was then used to prevent the low-pass filter circuit from loading the voltage divider circuit unacceptability and interfere with the frequency response of the filter. Implementation of the low-pass filter attenuates the fast switching pulse-width modulation (PWM) component of the signal. PWM is a technique used to relay data in the form of a varying pulse width, and is used to control power to the motor. The electronic circuit outputs a periodic waveform at the commutation frequency, which is the frequency of the switching of the polarity of the magnets to keep the motor turning. The highest peak of the spectrum of this signal is at the commutation frequency. Conversion from the commutation frequency  $f_c$  (Hz) to RPM is given by the formula  $\text{RPM} = f_c \cdot 60 \cdot 2 / N_p$ , where  $N_p$  is the number of magnetic poles in the motor. The EDF 70HW has four poles, for which  $\text{RPM} = 30f_c$ . The RPM inferred from the blade passing frequency measured by the microphones was within 0.5% of the RPM measured directly using the above method.

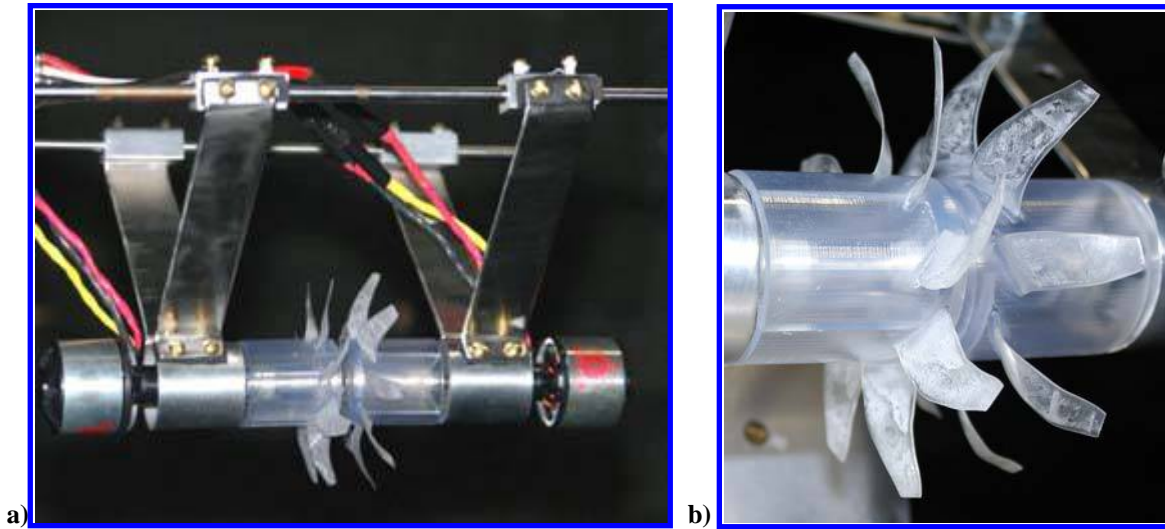


Fig. 5 Counter-rotating open rotor rig. a) Mounting mechanism; b) detail of rotors.

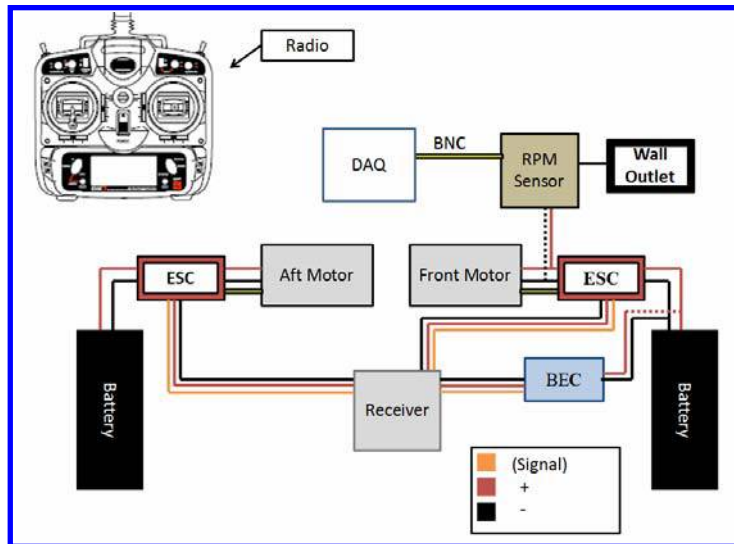


Fig. 6 Electronic circuitry.

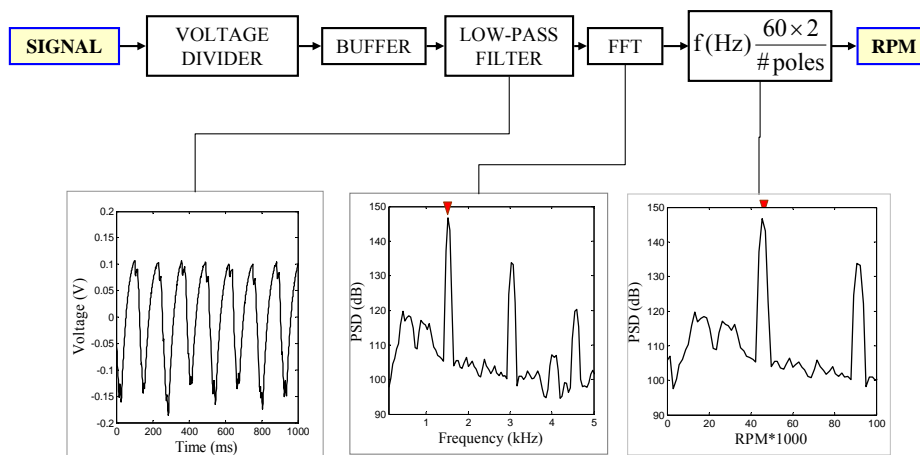


Fig. 7 Process for measurement of the rotor speed.



## B. Shielding Plate

Studies of rotor noise shielding utilized a rectangular aluminum plate of 3.2-mm thickness, 610-mm span, and variable chord. The shielding setup is shown in Fig. 8. The shield length downstream of the mid-rotor plane,  $X_{te}$ , was adjusted by translating the plate downstream while adding upstream segments so that the upstream shield length remained fixed at 127 mm. The downstream shield length was varied from 0 to 101.6 mm in increments of 25.4 mm (1.0 in). The blade tip clearance from the plate was 16 mm.

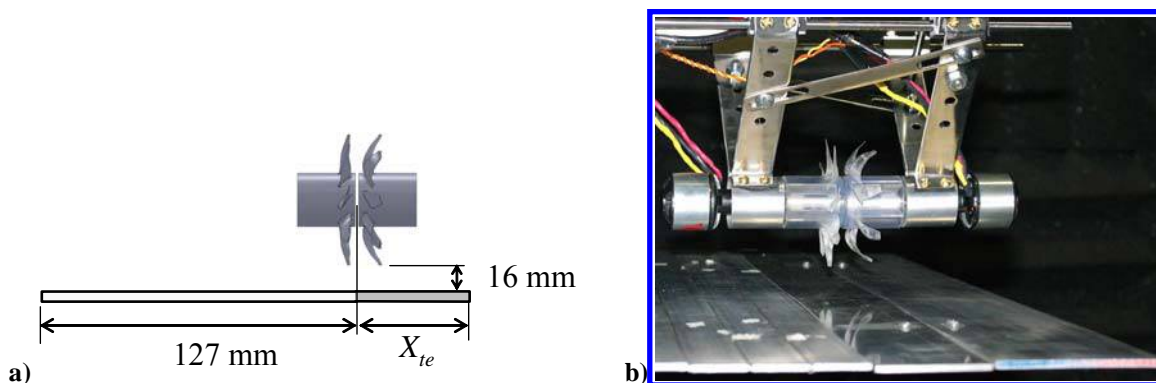


Fig. 8 Arrangement of shielding plate. a) Schematic of setup; b) picture of the layout.

## C. Aeroacoustic Testing

Acoustic surveys were conducted inside an anechoic chamber at the UC Irvine's Aeroacoustics Facility, depicted in Fig.9. The anechoic chamber houses twenty-four 3.2 mm condenser microphones (Bruel & Kjaer, Model 4138) with a frequency response of 140 kHz. The microphones were arranged twelve on a downward arm (azimuth angle  $\phi=0^\circ$ ) and twelve on a sideline arm (azimuth angle  $\phi=60^\circ$ ). On each arm, the measurement polar angle  $\theta$ , defined from the midpoint of the two rotors, ranged from  $20^\circ$  to  $120^\circ$  degrees relative to the downstream rotor axis. This arrangement enabled simultaneous measurement of the downward and sideline noise at all the polar angles of interest. Because of physical obstructions in the sideline path introduced by the support struts of the apparatus, only the downward data are relevant to this study.

The microphones were connected, in groups of four, to six conditioning amplifiers (Bruel & Kjaer, Model 2690-A-0S4). The 24 outputs of the amplifiers were sampled simultaneously, at 250 kHz per channel, by three eight-channel multi-function data acquisition boards (National Instruments PCI-6143). National Instruments LabView software was used to acquire the signals. The temperature and humidity inside the anechoic chamber were recorded to enable computation of the atmospheric absorption.

The number of samples for each test run was 262144. The narrowband sound pressure level spectra were computed with a Fast Fourier Transform size of 8192, giving a frequency resolution of 30.5 Hz. The SPL spectra were corrected for actuator response, free-field correction, and atmospheric absorption. The overall sound pressure level was calculated through integration of the SPL spectrum. The SPL spectrum and OASPL are referenced to a distance of 305 mm (12 in.) from the midpoint of the two rotors.

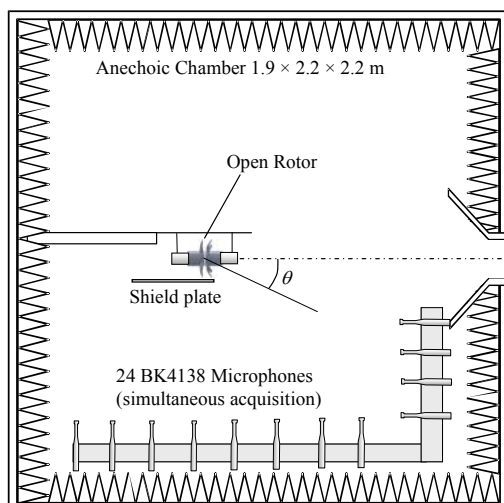


Fig.9 Aeroacoustic testing of open rotor.

#### IV. Results

This section presents acoustic results for the isolated rotor and the rotor in combination with the plate shield. Where feasible, comparisons with past data from large-scale tests are made. Table 1 presents the experimental matrix covered in this paper. The discussion will focus on the blade-passing-frequency (BPF) tones of the front and aft rotors,  $BPF_F$  and  $BPF_A$ , respectively, and their interactions. For conciseness, the following convention will be used in naming the tones:

$$\text{Tone } ij = i BPF_F + j BPF_A$$

Table 1 Experimental matrix

Type	FRONT ROTOR		AFT ROTOR		$X_{te}$ (mm)	$X_{te} / D$	UCI Exp.
	RPM	$M_{tip}$	RPM	$M_{tip}$			
Isolated	54900	0.67	*	*	-	-	ORM1101
Isolated	54900	0.67	46050	0.56	-	-	ORM1105
Shield	51300	0.62	46050	0.56	0.0	0	ORM1111
Shield	51300	0.62	46050	0.56	25.4	0.32	ORM1112
Shield	51300	0.62	46050	0.56	50.8	0.63	ORM1113
Shield	51300	0.62	46050	0.56	76.2	0.95	ORM1114
Shield	51300	0.62	46050	0.56	101.6	1.27	ORM1115

\* Unknown, propeller was unpowered and windmilling

##### A. Isolated Open Rotor

We examine first the acoustics with only the front rotor powered. The front rotor rotated at 54900 RPM or  $M_{tip}=0.67$ . The unpowered aft rotor windmilled at an unknown rotational speed (RPM measurement was possible only if the motor was powered). However, it is safe to assume that the rotational speed of the aft rotor was much smaller than that of front rotor, and thus the front rotor was the primary noise source. Figure 10 displays the far-field SPL spectrum near the rotor plane ( $\theta=94^\circ$ ) and in the aft direction ( $\theta=35^\circ$ ). Near the rotor plane, the fundamental BPF tone (10) and its higher harmonics, up to tone 50, are evident. The peak of tone 10 is 30 dB above the broadband noise. Examining the spectrum in the aft direction we distinguish clearly tones 10, 20, and 30. Higher harmonics are buried in the broadband noise. The tones are not as clean as for  $\theta=94^\circ$ , possibly because of interference with the windmilling aft rotor.

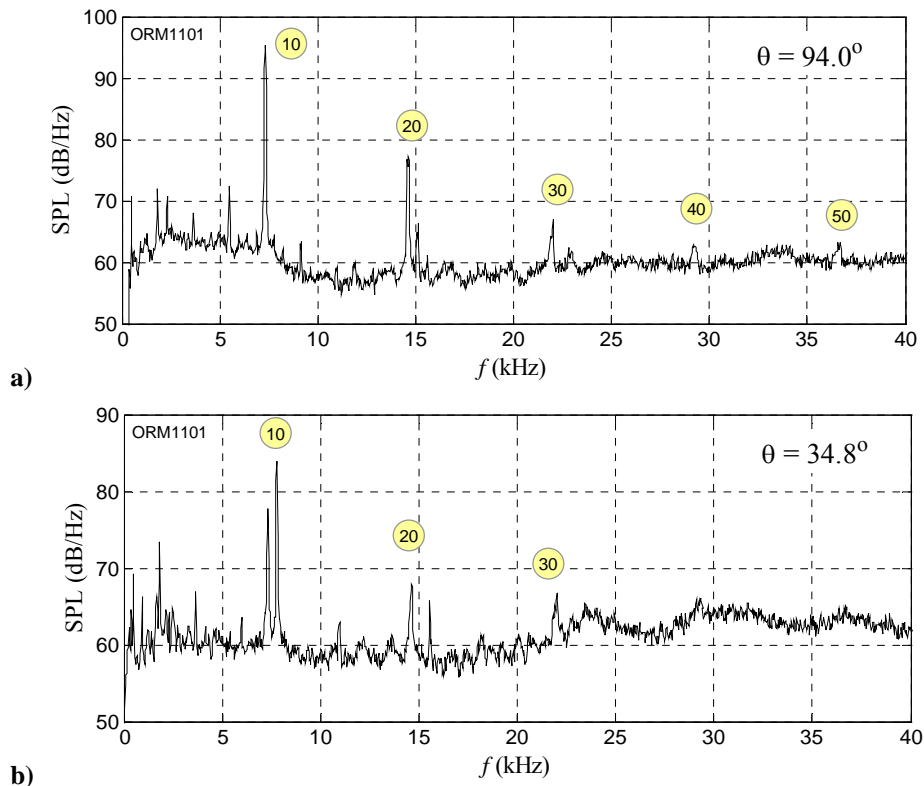


**Fig.10** Far-field narrowband SPL spectra for the isolated open rotor with only the front motor powered. a)  $\theta=94^\circ$ ; b)  $\theta=35^\circ$ .

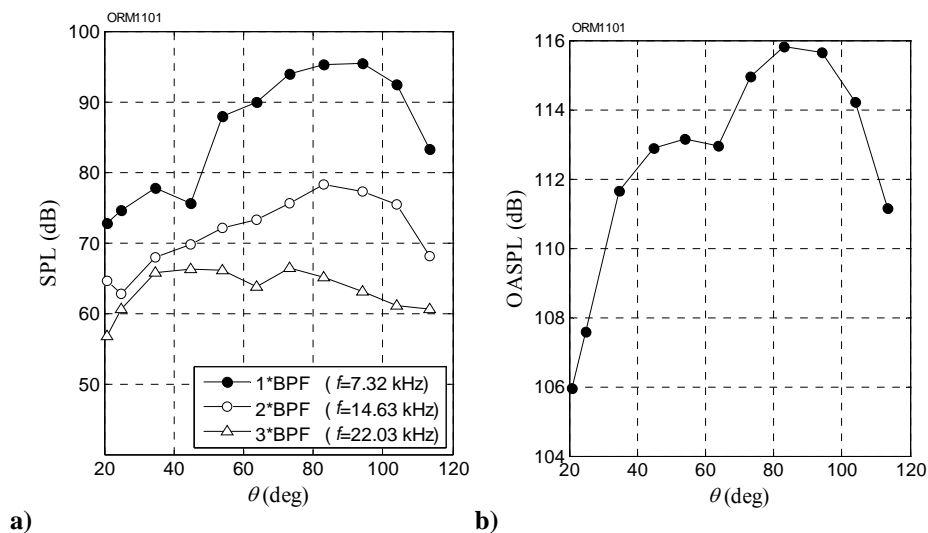


**Fig.11** Directivities of a) tones and b) OASPL for the isolated open rotor with only the front motor powered.

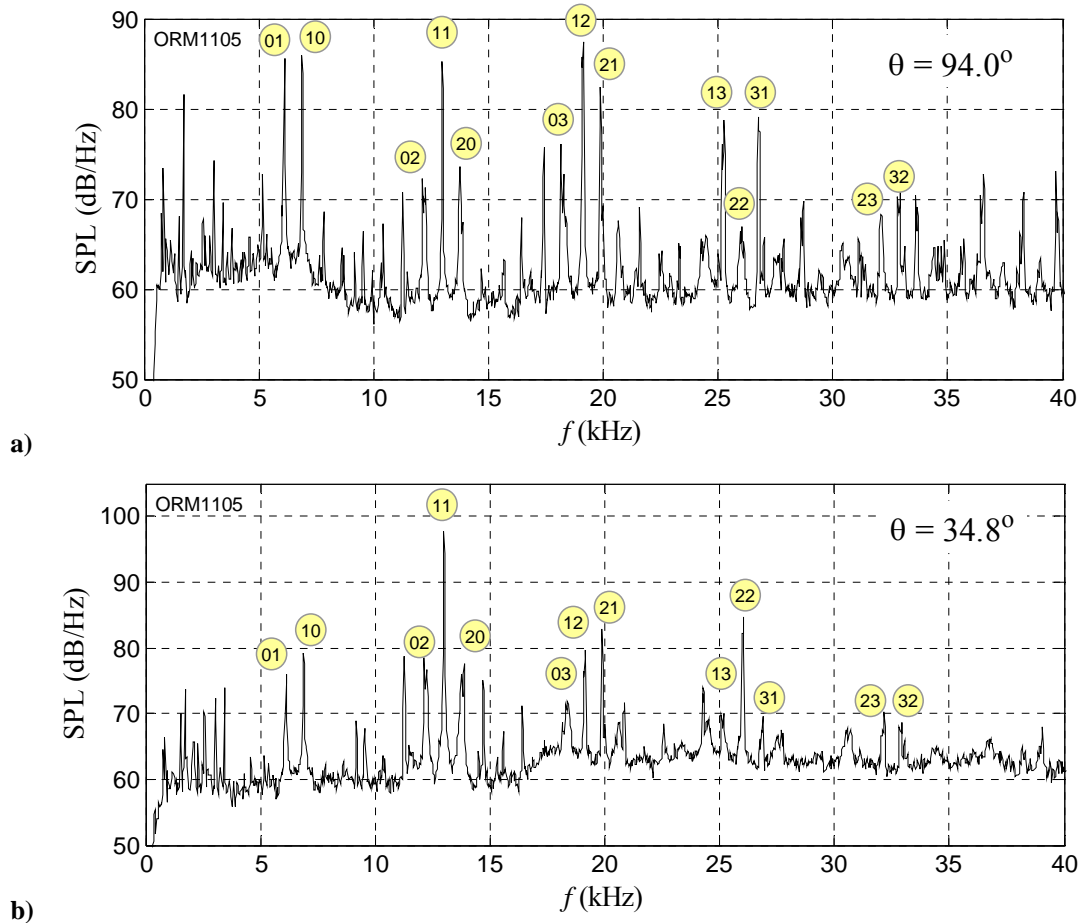
Figure 11 plots the directivities of tones 10, 20, and 30, and the directivity of the OASPL. The first two tones peak near the rotor plane, while tone 30 has a broad peak in the range  $30^\circ \leq \theta \leq 80^\circ$ . As expected, the OASPL peaks near the rotor plane.

We now examine the counter-rotating open rotor acoustics with both motors powered. The front rotor rotated at 51300 RPM ( $M_{tip}=0.62$ ) and the aft rotor rotated at 46050 RPM ( $M_{tip}=0.56$ ). The slower RPM of the aft rotor (10%



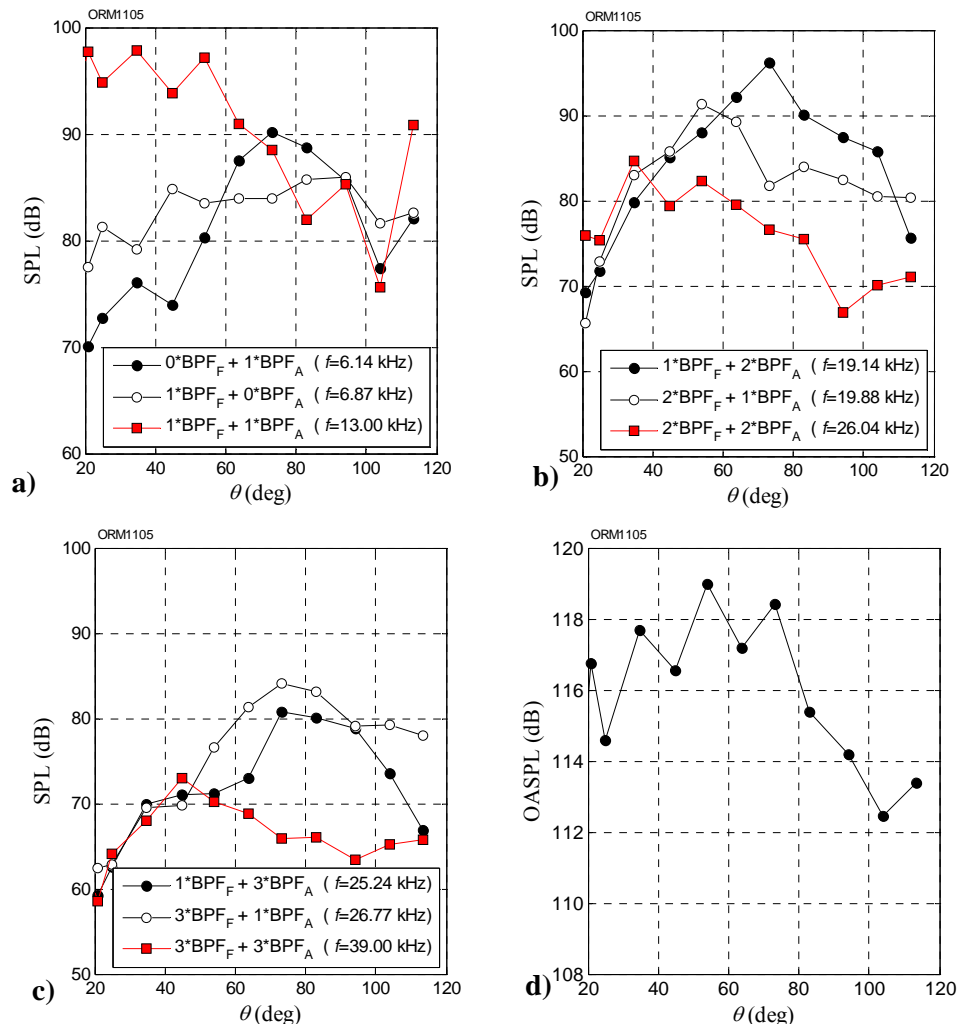
lower than the RPM of the front rotor) enables distinction of the fundamental tones of each rotor and their interactions. In addition, it allows qualitative comparisons with past large-scale experiments that had a similar speed setting<sup>6</sup>.

Figure 12 plots the far-field narrowband SPL spectra near the rotor plane ( $\theta=94^\circ$ ) and in the aft direction ( $\theta=35^\circ$ ). We observe a rich content of tones, with the principal ones labeled. Near the rotor plane, the fundamental BPF tones (01, 10) and interaction tones 11 and 12 are dominant and of similar magnitude. The next stronger tones are interaction tones 13 and 31, about 10 dB lower than the dominant tones. In the aft direction the interaction tone 11 dominates all the other tones by  $\sim 20$  dB. The next stronger tone is interaction tone 21, followed by tones 22 and 10. The dominance of interaction tones in the aft direction is a key feature of the counter-rotating rotor and presents critical challenges in shielding aft-emitted noise.



**Fig.12** Far-field narrowband SPL spectra for the isolated counter-rotating open rotor. a)  $\theta=94^\circ$ ; b)  $\theta=35^\circ$ .

The polar directivities of the principal tones and the OASPL are plotted in Fig. 13. The dominance of the interaction tone 11 in the aft direction is evident. For  $\theta < 100^\circ$ , the strength of tone 11 increases with decreasing polar angle. There is also a sharp increase with  $\theta > 100^\circ$ , although the trend that follows cannot be ascertained because the measurements end at  $\theta=113^\circ$ . Of the interaction tones involving 2\*BPF and 3\*BPF, tones 22 and 33 have flat directivities and are strong in the aft direction. It is thus expected that tones 11, 22, and 33 will be the most challenging to shield.



**Fig.13 Polar directivity of acoustics of counter-rotating open rotor: a) tones 01, 10, 11; b) tones 12, 21, 22; c) tones 13,31,33; and d) OASPL.**

It is instructive to compare the present results with those from large-scale tests of the F7/A7 8+8 rotor. Quantitative comparisons are not possible because the large-scale tests had a flight stream and the operating conditions were slightly different from the conditions in this study. Past data were extracted from Woodward and Hughes<sup>6</sup>. The diameters of the front and aft rotors were 622 mm and 607 mm, respectively, whereas the present experiment used the same diameter of 80 mm. The rotational speed of the aft rotor was 90% that of the front rotor, similar to the present experiment. The tip Mach numbers were 0.72 and 0.66 for the front and aft rotors, about 15% higher than the present values. The acoustics were measured in a tunnel with a freestream at Mach 0.2, versus the static environment of this study. Finally, the acoustic measurements were collected by microphones at a sideline distance of 1370 mm ( $\sim 2$  rotor diameters) whereas our data are in the far field at a distance of at least 10 rotor diameters.

Fig.14a reproduces the narrowband spectrum in the polar direction  $\theta=108^\circ$ . The similarity with the small-scale spectrum of Fig.12a is evident. Fig. 14b presents an approximate reconstruction of tones 01, 10, and 11, and can be compared to Fig. 13a. Even though the relative levels are different, there is general agreement of the directivity trends, particularly for the interaction tone 11 whose amplitude is low at the rotor plane and amplifies in the aft direction.

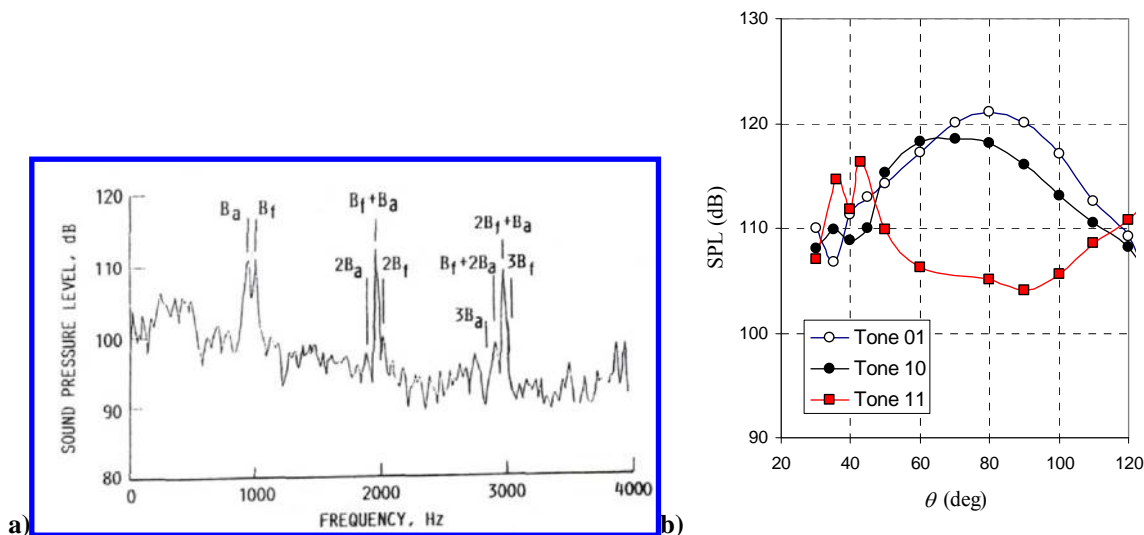


**Fig.14** Reproduction and approximate reconstruction of past acoustic results of F7/A7 8+8 open rotor<sup>6</sup>. a) Narrowband SPL spectrum at  $\theta=108^\circ$  (Fig. 7 of Ref. 6); approximate directivity of rotor-alone and interaction tones (from Figs. 10, 11, and 13 of Ref.6).

## B. Shielded Open Rotor

We examine the impact of the shield of Fig. 8 on the far-field acoustics. Figure 15 presents narrowband far-field spectra at  $\theta=94^\circ$  for the isolated rotor and for the shielded rotor with  $X_{te}/D=0.63$  and 1.27. With increasing downstream shield length there is a significant reduction of the broadband level. There is a general reduction of the tones although it is non-uniform and not necessarily monotonic. A few tones actually amplify. Tone 22, one of the weaker tones for the isolated rotor, amplifies by about 5 dB for  $X_{te}/D=1.27$ . Because the overall levels drop, tone 22 becomes the second dominant tone (after tone 11) at  $X_{te}/D=1.27$ . In addition, tones that do not fall under rotor-alone or interaction tones amplify with insertion of the shields, such as the tones at  $f=11.2$  kHz and 14.7 kHz, indicated with red triangles in Fig. 15. The spectral changes at  $\theta=35^\circ$  are shown in Fig. 16. Predictably, the overall reduction is less than at  $\theta=94^\circ$ . The dominance of interaction tone 11 is evident. It is interesting to note that tone 11 is reduced for  $X_{te}/D=0.63$  but reappears strong for  $X_{te}/D=1.27$ . Figures 15 and 16 indicate that, although significant overall shielding occurs, the behavior of the tonal components is very complex and defies simple trends.

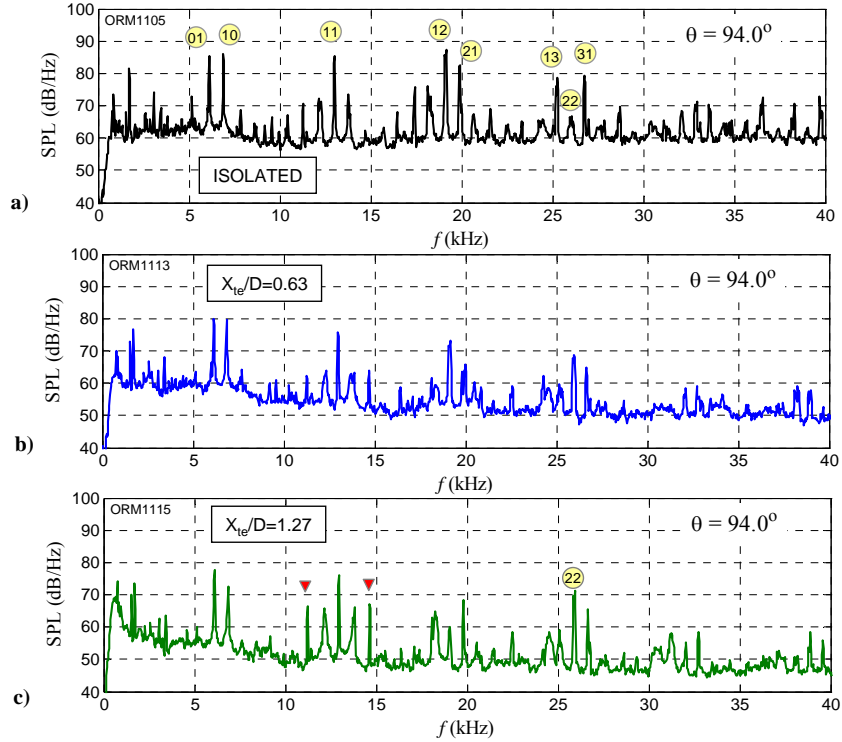


**Fig.15** Narrowband SPL spectra at  $\theta=94^\circ$  for counter-rotating rotor. a) Isolated; b) plate shield with  $X_{ie}/D=0.63$ ; c) plate shield with  $X_{ie}/D=1.27$ .

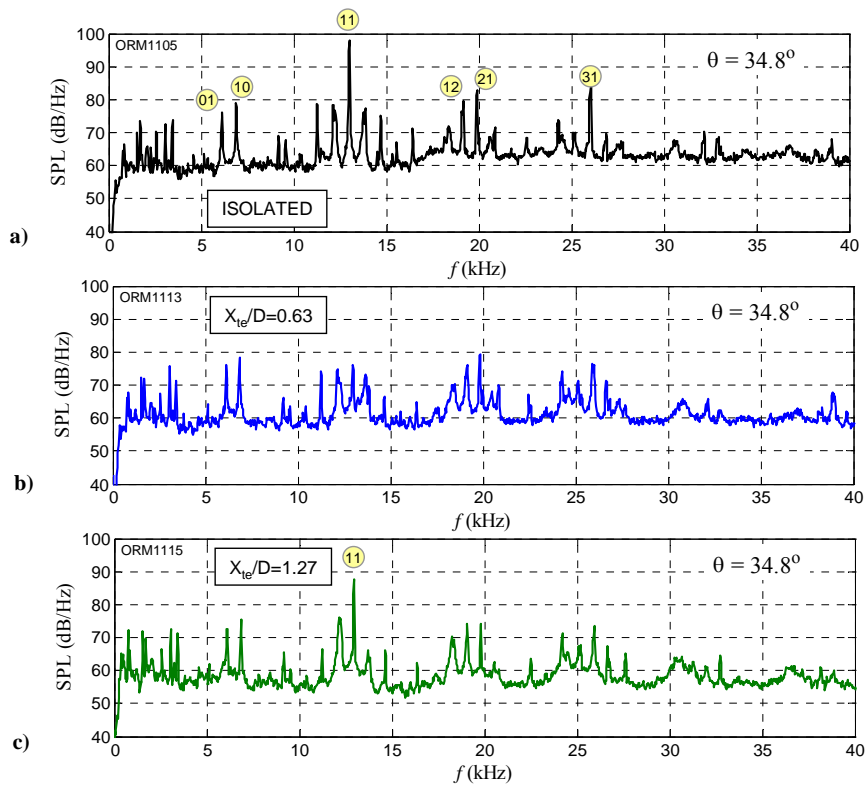


**Fig.16** Narrowband SPL spectra at  $\theta=35^\circ$  for counter-rotating rotor. a) Isolated; b) plate shield with  $X_{ie}/D=0.63$ ; c) plate shield with  $X_{ie}/D=1.27$ .

Figure 17 plots the directivities of some of the principal tones for different shield lengths and compares them to the corresponding directivities of the isolated rotor. For the tones that peak near the rotor plane (such as tones 10, 01, 21, and 12) the shield with  $X_{te}/D \geq 0.64$  provides significant attenuation of the peak levels, on the order of 10-15 dB; smaller shield lengths ( $X_{te}/D = 0, 0.32$ ) provide marginal reductions, even in the forward arc. For the tones that peak in the aft arc, or for the tones that amplify, the shield is much less effective in reducing noise. For interaction tone 11 (Fig. 17c) there is virtually no reduction near  $\theta = 25^\circ$ , even with the long shield length of  $X_{te}/D = 1.27$ . The same observation applies to tone 22 (Fig. 17f) at low polar angles. Interestingly, tone 22 is not suppressed near  $\theta = 90^\circ$  due to its amplification with increasing shield length, as noted in the discussion of Fig. 16. Finally, Fig. 18 shows the impact of the shield on the directivity of the OASPL. Significant reductions are noted; however, these do not necessarily reflect the impact on aircraft noise due to the complexity of the tonal directivity discussed above.

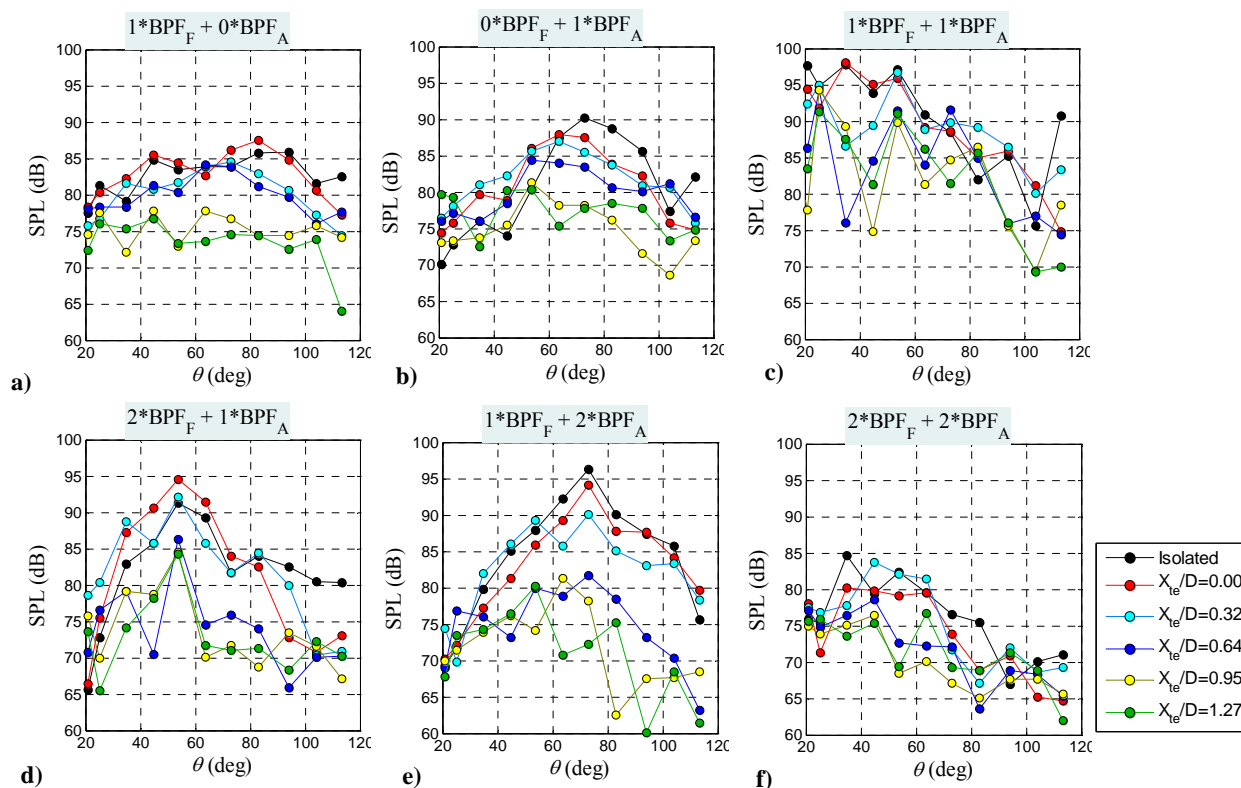


**Fig.17** Directivity of tones of counter-rotating open rotor in isolation and with the plate shield. a) Tone 10; b) tone 01; c) tone 11; d) tone 21; e) tone 12; and f) tone 22.

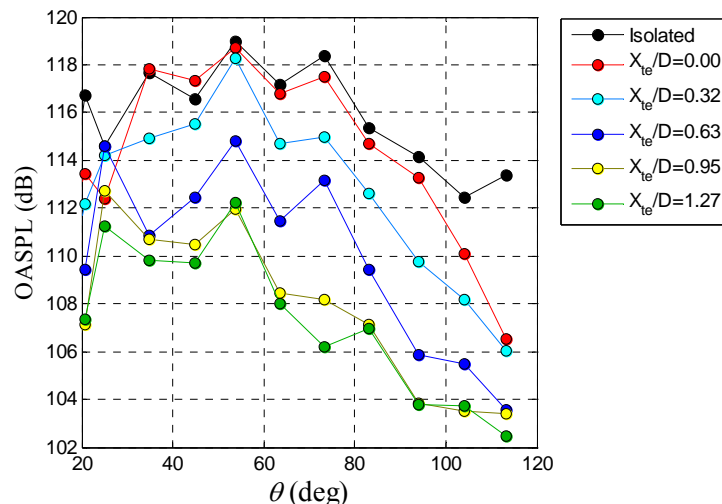


Fig.18 Directivity of OASPL for isolated and shielded open rotors.

## V. Concluding Remarks

This study examined the potential of very-small-scale experiments to simulate the acoustics of large scale counter-rotating open rotors in isolation and with a rectangular-plate shield. The experimental rotor model was based on the historical F7/A7 design developed by General Electric. The 80-mm diameter rotors were fabricated using advanced stereolithography and were powered by two high-performance DC brushless motors. Realistic tip Mach numbers were achieved with the rotors spinning near 50000 rpm. Far-field acoustic surveys were conducted inside an anechoic chamber using a 12-microphone array. The isolated tests captured the tonal and broadband contents of open rotor noise. Rotor-alone tones dominated the sound emission in the vicinity of the rotor plane. In the aft direction, interaction tones were very strong. Addition of the rectangular plate shield created complex trends in the tonal content. Tones radiating in the direction of the rotor plane were well attenuated, while tones emitted in the aft direction were poorly shielded. Some tones were amplified with insertion of the shield. Even though the shield reduced the noise level in an overall sense, the complicated tonal pattern presents challenges for the effective reduction of aircraft noise.

In assessing the simulation parameters for rotor tests at the very small scale, the paramount criterion is attaining realistic rotor tip speeds. The present study shows that this is technically feasible. Next are the issues of trailing edge thickness, Reynolds number, and forward flight. The trailing edge thickness is an issue of materials and fabrication technology; it is likely to improve somewhat in the future, although it is safe to assume that the relative thickness will be larger than in a large-scale test. Therefore, thickness noise should be evaluated systematically to assess the conditions under which results of very-small-scale tests may be problematic. Regarding effects of Reynolds number, in the present tests the Reynolds number based on the conditions near the rotor tip was around  $10^5$ , a regime that likely results in a laminar boundary layer, the latter expected in the full-scale application. In large-scale tests, such as in Ref.6, the Reynolds number is on the order of  $10^6$ , a transitional regime which could in fact be more problematic than a purely laminar or purely turbulent boundary layer, the latter expected in the full-scale application. The lack of forward-flight capability is connected to the present facility and it not a generic limitation of small-scale rigs. Finally, there are obvious improvements to the existing setup that would have produced a cleaner testing environment, such as refining the support structure for the rotors. These were not pursued due to the very limited resources of this project.

It is again emphasized that very-small scale tests would not replace the experiments in large and richly instrumented facilities. Rather, they may serve as a filtering tool so that large-scale tests are used most efficiently and economically. They also present an opportunity for basic research at costs typical of university projects. The results presented here support this concept.



## References

1. Groeneweg, J. and Bober, L., "NASA Advanced Propeller Research," NASA TM-101361, September 1988.
2. General Electric Aircraft Engines, "Full Scale Technology Demonstration of a Modern Counter Rotating Unducted Fan Engine. Design Report," NASA Design Report CR-180867, December 1987.
3. Strack, W., Knip, G., Weisbrich, A.L., Godston, J., and Bradley, E., "Technology and Benefits of Aircraft Counter-Rotation Propellers," NASA Technical Memorandum 82983, October 1982.
4. Sullivan, W.E., Turnberg, J.E., and Violette, J.A., "Large-Scale Advanced Prop-Fan (LAP) Blade Design," NASA Technical Report CR-174790, 1984.
5. Woodward R.P., "Noise of a Model High Speed Counter Rotation Propeller at Simulated Takeoff/Approach Conditions (F7/A7)," NASA TM-100206, October 1987.
6. Woodward, R.P. and Hughes, C.E., "Aeroacoustic Effects of Reduced Aft Tip Speed at Constant Thrust for a Model Counterrotation Turboprop at Takeoff Conditions," AIAA Paper 90-3933, October 1990.
7. Parry, A.B., Kingan, M., and Tester, B.J., "Relative importance of Open Rotor Tone and Broadband Noise Sources," AIAA 2011-2763, June 2011.
8. Pankratov, I.V., Samokhin, V.F., Vlasov, E.V., Chevagin, A.F., "Acoustic Test of Contra Rotating Propellers in the Dream project," AIAA 2011-2761, June 2011.
9. Stuermer A. and Yin J., "Low-Speed Aerodynamics and Aeroacoustics of CROR Propulsion Systems," AIAA Paper 2009-3134, May 2009.
10. Berton, J.J., "Empennage Noise Shielding Benefits for an Open Rotor Transport," AIAA 2011-2764, June 2011.
11. Stephens, D.B., and Envia, E., "Acoustic Shielding for a Model Scale Counter-rotating Open Rotor," AIAA Paper 2011-2940, June 2011.
12. Pitera, D.M., DeHaan, M., Brown, D., Kawai, R.T., Hollowell, S., Camacho, P., Bruns, D., and Rawden, B.K., "Blended Wing Body Concept Development with Open Rotor Engine Integration," NASA/CR-2011-217303, November 2011.
13. Czech, M.J. and Thomas, R.H., "Experimental Studies of Open Rotor Installation Effects," AIAA Paper 2011-4047, June 2011.
14. Papamoschou D. and Mayoral S., "Jet Noise Shielding for Advanced Hybrid Wing-Body Configurations," AIAA Paper 2011-0912, January 2011.